Direct numerical simulation (DNS) modeling of PEFC electrodes
Part I. Regular microstructure

Guoqing Wang [1], Partha P. Mukherjee, Chao-Yang Wang *

Electrochemical Engine Center (ECEC) and Department of Mechanical & Nuclear Engineering, The Pennsylvania State University, University Park, PA 16802, USA

Abstract

A direct numerical simulation (DNS) model is developed to achieve pore-level description of polymer electrolyte fuel cell (PEFC) electrodes. The DNS method solves point-wise accurate conservation equations directly on an electrode microstructure comprising of various phases and hence utilizes the intrinsic transport properties of each phase. Idealized two- and three-dimensional regular microstructures are constructed to represent the porous cathode catalyst layer. Various voltage losses identified from the simulation results are compared with experimental observations. This pore-scale model is further applied to study the morphological effects, such as pore size, layer thickness and porosity, on the performance of the cathode catalyst layer.
© 2005 Elsevier Ltd. All rights reserved.

Keywords: Polymer electrolyte fuel cell; Cathode catalyst layer; Pore-level description; Direct numerical simulation (DNS)

1. Introduction

In polymer electrolyte fuel cells (PEFC), two thin electrodes, usually referred to as the catalyst layers (CL), are attached to an ionomeric membrane, typically Nafion®, to form the membrane electrode assembly (MEA), which constitutes the heart of a fuel cell. The fuel (i.e. hydrogen) and oxidant (i.e. oxygen) react electrochemically in the active catalyst layers to produce electricity, water and waste heat. The hydrogen oxidation reaction (HOR) occurs in the anode catalyst layer, while oxygen reduction reaction (ORR) takes place in the cathode catalyst layer. Despite significant developments, major voltage losses in the PEFC include sluggish kinetics of the ORR and transport limitations of protons and oxidizing species in the cathode catalyst layer. Therefore, it is imperative to fully understand pore-level phenomena taking place in the cathode catalyst layer.

A typical cathode catalyst layer of a PEFC consists of a solid matrix of Pt/carbon particles providing pathways for electron conduction to the reaction site, an ionomer network providing pathways for proton transport and a network of open pores for oxygen and product water transport. Additionally, the ionomer acts as a binder for the structure and provides stability and mechanical strength to the catalyst layer. The electrochemical reaction takes place at the triple-phase boundary forming an active catalyzed interface, where oxygen is consumed together with protons and electrons, producing water along with waste heat. The cathodic half-reaction, i.e. the ORR, is given by:

$$O_2 + 4H^+ + 4e^- \rightarrow 2H_2O \qquad (1)$$

Thus, the cathode catalyst layer is a complex porous structure comprising of three phases. An excellent account on the structures and functions of the catalyst layer was given by Gottesfeld and Zawodzinski [1].

Various modeling approaches have been used for catalyst layers. In most of the macroscopic models in the literature [2–5], developed for the polymer electrolyte fuel cell, the active catalyst layer was not the main focus, rather treated either as an ultra-thin layer in terms of an interface or as a macrohomogeneous porous layer. Essentially based on the theory of volume averaging, these models specifically developed for PEFC catalyst layers, can be further categorized as a homogeneous model, a film model and an agglomerate model. Springer and Gottesfeld [6], Eikerling and Kornyshev [7], Perry et al. [8] presented

---

* Corresponding author. Tel.: +1 814 863 4762; fax: +1 814 863 4848.
 E-mail address: cxw31@psu.edu (C.-Y. Wang).
[1] Present address: Plugpower Inc., 968 Albany-Shaker Road, Latham, NY 12110, USA.

some comprehensive analytical and numerical solutions for the cathode catalyst layer under various conditions. Recently, Wang [9] and Weber and Newman [10] provided excellent overviews of the various catalyst layer models.

However, these models do not address the local pore-scale phenomena. In their work, Pisani et al. [11] constructed an analytical pore-scale model to study the effects of catalyst layer pore structure on performance over idealized, one-dimensional (1-D) pore geometry. Their emphasis was to ascertain the pore-scale phenomena, for example, the variation of the reactant concentration within the electrolyte phase at the pore-level and decouple these primary variables varying at the pore-level from the ones, which show no pore-scale variation. Preferential non-homogeneity was inducted into the model by defining an effective reaction rate through a modified analytical expression of the Butler–Volmer equation deduced separately for each of the simplified geometries under consideration. Although, they tried to show the effect of the non-homogeneous porous structure through partly accounting for the modified reaction rate, their approach lacked a unified pore-level description of the species and charge transport. The objective of the present work is to demonstrate, for the first time, the development and implementation of a direct numerical simulation (DNS) model on idealized two- and three-dimensional (2- and 3-D) catalyst layer microstructures and assess the effects of morphological parameters on the performance of the cathode catalyst layer through a systematic pore-scale description of the underlying transport processes.

2. DNS model

The DNS model has essentially two steps: the first step is the construction of the catalyst layer microstructure describing the underlying micro-morphology comprising of various phases and the next step is to solve the transport equations for charge and species conservation directly on the microstructure. For the ORR to occur, a typical cathode catalyst layer is assumed to consist of uniformly dispersed Pt particles between the electronic phase (i.e. carbon) and the electrolyte phase (i.e. Nafion®) forming an active reaction interface, which is further accessible, by oxygen. Various symbols used in the following subsections are defined in the nomenclature.

2.1. Idealized 2-D microstructure

According to the basic features of the catalyst layer microstructure described above, a 2-D realization of it is constructed as shown in Fig. 1. In the schematic diagram, x-direction is across the catalyst layer thickness and y-direction represents a periodic repeating unit of the actual catalyst layer. In the physical system, a thin film of ionomer is assumed to exist between the electronic phase and the gas phase forming an active catalyzed interface. Protons migrate into the CL from the membrane side on the left boundary (i.e. $x = 0$) and oxygen diffuses into the layer through the gas diffusion layer (GDL) on the right boundary (i.e. $x = x_L$). Oxygen thereafter dissolves in the electrolyte film and is consumed at the catalyzed interface along with protons and elec-
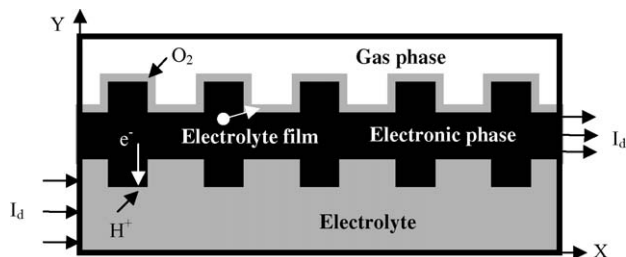
Fig. 1. Schematic diagram of the 2-D computational domain.

trons due to the ORR. The catalyst layer thickness is considered to be 20 μm in the present study.

2.1.1. Model assumptions

As a first step toward modeling the cathode catalyst layer using the DNS approach, the following assumptions are made:

- At the reaction interface, thermodynamic equilibrium is assumed to exist between the oxygen concentration in gas phase and that dissolved in the electrolyte phase. O_2 diffusion resistance through the electrolyte film is ignored due to the small thickness of the film (estimated to be ~5 nm).
- The mass balance of product water is not considered, assuming that water is in the gas phase due to heat generation in the CL and diffuses out of CL sufficiently fast. This assumption may bring considerable error at large current densities, which will be justified later.
- The proton conductivity in the electrolyte phase is treated as a constant, though it actually depends on the water content in the ionomer.
- Isothermal and steady state operation.

2.1.2. Governing equations

A single set of governing differential equations valid for all the phases is developed; therefore, no internal boundary condition is required to be specified at the phase interfaces. Due to slow kinetics of the ORR, the rate of electrochemical reaction assumes Tafel kinetics as:

$$j = -i_0 \frac{c_{O_2}}{c_{O_2,ref}} \exp\left(\frac{\alpha_c F}{RT}\eta\right) \tag{2}$$

The overpotential, η, is defined as:

$$\eta = \phi_s - \phi_e - V_{oc} \tag{3}$$

where ϕ_s and ϕ_e stand for the electronic and electrolyte phase potentials at the reaction sit, respectively. V_{oc} is the reference open-circuit potential of the cathode under the specified operation temperature.

The charge conservation for electron and proton and oxygen conservation equations can be described, respectively, as:

$$\nabla \cdot (\sigma \nabla \phi_s) + a \int_\Gamma j\delta(x - x_{interface})ds = 0 \tag{4}$$

$$\nabla \cdot (\kappa \nabla \phi_e) + a \int_\Gamma j\delta(x - x_{interface})ds = 0 \tag{5}$$

$$\nabla.(D\nabla c_{O_2}) + a \int_\Gamma \frac{j}{4F}\delta(x - x_{\text{interface}})\mathrm{d}s = 0 \qquad (6)$$

where the transfer current density, j, is positive for the electronic phase and negative for the electrolyte phase since current is transferred from the electronic phase into the electrolyte. σ and κ represent electronic conductivity and electrolyte conductivity, respectively and D refers to the oxygen diffusivity in the gas phase. Also, a represents the specific interfacial area and is defined as the interfacial surface area, where the reaction occurs per unit volume of the catalyst layer, s is the interface, Γ represents the interfacial surface over which the surface integral is taken, $\delta(x - x_{\text{interface}})$ is a delta function which is zero everywhere but unity at the interface, where the reaction occurs.

2.1.3. Model boundary conditions

On the left boundary, a constant current density, i_d, is applied through the electrolyte phase, while it is transferred out of the electronic phase on the right boundary. A constant oxygen concentration equal to the value at the channel inlet is assumed on the right boundary. The boundary conditions can, therefore, be summarized as follows:

$$c_{O_2} = c_{O_2,0}, \qquad \text{in the gas phase, at } x = x_L \qquad (7)$$

$$-\sigma \frac{\partial \phi_e}{\partial x} = i_d, \qquad \text{in the electrolyte phase, at } x = 0 \qquad (8)$$

$$-\kappa \frac{\partial \phi_s}{\partial x} = i_d, \qquad \text{in the electronic phase, at } x = x_L \qquad (9)$$

$$\frac{\partial c_{O_2}}{\partial n} = 0, \quad \frac{\partial \phi}{\partial n} = 0, \quad \text{everywhere on the other boundaries} \qquad (10)$$

2.1.4. Solution procedure

The governing partial differential equations are discretized using the control volume-based finite difference method by Patankar [12] and the resulting set of algebraic equations are iteratively solved. The number of cells used in the simulations is 160 in the x-direction and 24 in the y-direction. The input parameters, including the properties of each phase, are given in Table 1. The equations are solved simultaneously and convergence is considered to be reached, when the relative error in each field between two consecutive iterations is less than 10^{-5}.

2.2. Three-dimensional regular microstructure

It should be noted that the idealized two-dimensional microstructure shown in Fig. 1 has some departure from reality. For instance, the reaction area obviously seems to be much less than that in a real 3-D catalyst layer, in which case the reaction area is roughly 100 times larger than the nominal electrode cross-sectional area. To demonstrate the concept and utility of the DNS approach in assessing the effects of the micro-morphology on pore-scale diffusion and reaction, a three-dimensional microstructure is, therefore, constructed to apply the DNS model, as shown in Fig. 2. Here, the catalyst layer is simplified to contain two phases, the gas phase

Table 1
Model input parameters

Parameter	Solid phase	Electrolyte phase	Gas phase
Conductivity, σ (S/cm)	50	0.05	0
O_2 diffusion coefficient, D (cm^2/s)	0	0	0.01
Inlet pressure (kPa)	150		
Reference concentration (mol/cm^3)	51.1×10^{-6}		
Temperature, T (°C)	80		
Catalyst layer thickness (μm)	20		
CL domain size in the periodic planes (μm)	3		
Electronic phase volume fraction, ε_s	0.5		
Electrolyte phase volume fraction, ε_e	0.25		
Gas phase volume fraction, ε_g	0.25		
Exchange current density, i_0 (A/cm^2)	1.0×10^{-8}		
Cathodic transfer coefficient, α_c	1.0		
Open-circuit potential, V_{oc} (V)	1.1		

and a mixed electrolyte/electronic phase. On the left boundary, protons migrate into the CL from the membrane and on the right boundary, oxygen and electrons transport into the layer through the GDL. The catalyst layer to be considered typically ranges from 10 to 20 μm thick and the pore size is about one to two orders-of-magnitude smaller. In the present study, the pore size is approximately specified by the elementary cell size in the computational domain. In the y–z-directions, the computational domain is assumed to have symmetry boundary conditions such that many repeating units form the entire catalyst layer.

2.2.1. Model assumptions

Pertinent assumptions made additionally to the 3-D simulation of the CL are as follows:
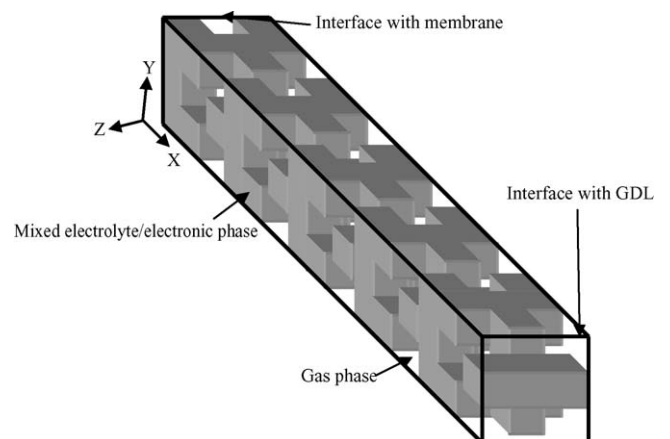
Fig. 2. Schematic diagram of the 3-D catalyst layer structure.

- The electronic phase potential is assumed to be uniform because the electrode is very thin and its electronic conductivity is sufficiently high. Thus, electron transport does not need to be considered. Under this assumption, the mixed phase is treated as the electrolyte phase and the ionic conductivity is duly corrected with respect to the mixed phase volume fraction using Bruggeman correlation as follows:

$$\kappa = \kappa_0 \cdot \left(\frac{\varepsilon_e}{\varepsilon_e + \varepsilon_s} \right)^{1.5} = \kappa_0 \cdot \left(\frac{\varepsilon_e}{1 - \varepsilon_g} \right)^{1.5} \tag{11}$$

where κ_0 is the intrinsic conductivity of the electrolyte, and ε_e, ε_s and ε_g are the electrolyte, electronic and pore volume fractions, respectively. In this study, the ratio of the electrolyte phase volume fraction to that of the electronic phase is fixed at unity and κ_0 is assumed constant. Henceforth, for simplicity, the mixed phase is referred to as the electrolyte phase.

- The interface between the gas phase and the mixed phase is assumed to be completely catalyzed and activated by platinum nanoparticles. The entire interface is, therefore, electrochemically active for the ORR.

2.2.2. Governing equations

Under the assumptions already stated, the governing equations for charge transport in the electrolyte phase and oxygen transport in the gas phase, respectively, are:

$$\nabla \cdot (\kappa \nabla \phi_e) + a \int_\Gamma j \delta(x - x_{\text{interface}}) ds = 0 \tag{12}$$

the governing equations are extended to the entire computational domain by incorporating a phase function f. The phase function is defined as unity in the electrolyte phase and zero in the gas phase, respectively. The proton conductivity and oxygen diffusivity can be generally expressed, at each elementary cell center, in the discretized sense, as:

$$K(i, j, k) = \kappa \cdot f(i, j, k) \tag{14}$$

$$D(i, j, k) = D_{O_2}^g \cdot [1 - f(i, j, k)] \tag{15}$$

The transfer current between the two neighboring cells at the phase interface, shown in Fig. 3, is given by the Tafel equation as follows:

$$j = i_0 \frac{c_{O_2}(i + 1, j, k)}{c_{O_2,\text{ref}}^g} \exp \left[\frac{\alpha_c F}{RT} \phi_e(i, j, k) \right] \tag{16}$$

where $\phi_e(i, j, k)$ has been used to represent the cathodic overpotential in the kinetic expression since both the open-circuit potential and the electronic phase potential are constant. It should be noted that the prefactor, i_0, is the modified exchange current density after replacing overpotential, η, in Eq. (2) with the expression given by Eq. (3). The control volume, with cell center (i, j, k), has six interfaces with the neighboring cells, where the electrochemical reaction might occur. The sum of the flux from all the reactions can be expressed as the volumetric source term. Therefore, the source/sink terms in Eqs. (12) and (13) can be replaced with discretized terms, S_ϕ and S_{O_2}, respectively, at the cell center (i, j, k) and can be expressed as:

$$S_\phi(i, j, k) = -\frac{i_0}{c_{O_2,\text{ref}}^g} f(i, j, k) \exp \left[\frac{\alpha_c F}{RT} \phi_e(i, j, k) \right] \cdot \left\{ [1 - f(i, j, k)] \frac{c_{O_2}(i - 1, j, k)}{\Delta x} + [1 - f(i + 1, j, k)] \frac{c_{O_2}(i + 1, j, k)}{\Delta x} \right.$$

$$+ [1 - f(i, j - 1, k)] \frac{c_{O_2}(i, j - 1, k)}{\Delta y} + [1 - f(i, j + 1, k)] \frac{c_{O_2}(i, j + 1, k)}{\Delta y} + [1 - f(i, j, k - 1)] \frac{c_{O_2}(i, j, k - 1)}{\Delta z}$$

$$+ [1 - f(i, j, k + 1)] \frac{c_{O_2}(i, j, k + 1)}{\Delta z} \left. \right\} \tag{17}$$

$$S_{O_2}(i, j, k) = -\frac{i_0}{4F c_{O_2,\text{ref}}^g} [1 - f(i, j, k)] c_{O_2}(i, j, k) \cdot \left\{ f(i - 1, j, k) \exp \left[\frac{(\alpha_c F/RT)\phi_e(i - 1, j, k)}{\Delta x} \right] \right.$$

$$+ f(i + 1, j, k) \exp \left[\frac{(\alpha_c F/RT)\phi_e(i + 1, j, k)}{\Delta x} \right] + f(i, j - 1, k) \exp \left[\frac{(\alpha_c F/RT)\phi_e(i, j - 1, k)}{\Delta y} \right]$$

$$+ f(i, j + 1, k) \exp \left[\frac{(\alpha_c F/RT)\phi_e(i, j + 1, k)}{\Delta y} \right] + f(i, j, k - 1) \exp \left[\frac{(\alpha_c F/RT)\phi_e(i, j, k - 1)}{\Delta z} \right]$$

$$+ f(i, j, k + 1) \exp \left[\frac{(\alpha_c F/RT)\phi_e(i, j, k + 1)}{\Delta z} \right] \left. \right\} \tag{18}$$

$$\nabla \cdot (D_{O_2}^g \nabla c_{O_2}) + a \int_\Gamma \frac{j}{4F} \delta(x - x_{\text{interface}}) ds = 0 \tag{13}$$

The second term in both the equations represents a source/sink term only at the electrochemically active interface where the ORR takes place.

In order to facilitate numerical solution of Eqs. (12) and (13) without resolving the microscopically complex phase interface,

From Eq. (17), it is apparent that only the electrolyte phase, with the phase function f of unity, has a non-zero source term for charge transport when there is a gas phase next to it. Similarly, in Eq. (18), only the gas phase cell having neighboring electrolyte phase cells has a source term due to oxygen consumption.

2.2.3. Boundary conditions

The computational domain for 3-D simulations is schematically shown in Fig. 4. Basically, only one quarter of the full
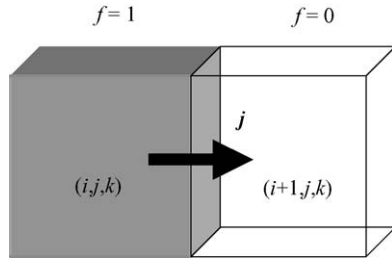
Fig. 3. The transfer current between two adjacent cells.

domain, shown in Fig. 2, is considered due to the symmetry in y- and z-directions. The computational domain extent is $20\,\mu m \times 3\,\mu m \times 3\,\mu m$. At the left boundary, where the protons migrate from the membrane, one cell layer of all electrolyte phase is added to the computational domain. The operating current density is uniformly applied to this additional layer, making the boundary condition straightforward to be implemented. Likewise, one cell layer of all gas phase is applied at the right boundary, which supplies oxygen at a constant concentration. In summary, the boundary conditions are described as,

At $y = 0$, $y = y_L$, $z = 0$, $z = z_L$:

$$\frac{\partial c_{O_2}}{\partial n} = 0, \qquad \frac{\partial \phi_e}{\partial n} = 0 \tag{19}$$

At the left boundary (i.e. the membrane–CL interface):

$$x = 0, \qquad \frac{\partial c_{O_2}}{\partial n} = 0, \qquad -\kappa \frac{\partial \phi_e}{\partial n} = i_d \tag{20}$$

At the right boundary (i.e. the CL–GDL interface):

$$x = x_L, \qquad c_{O_2} = c_{O_2,0}, \qquad \frac{\partial \phi_e}{\partial n} = 0 \tag{21}$$

2.2.4. Model input parameters

The input parameters including the transport and kinetic parameters used in the three-dimensional study are mainly taken from Table 1 in order to compare the results with those from the two-dimensional prediction.
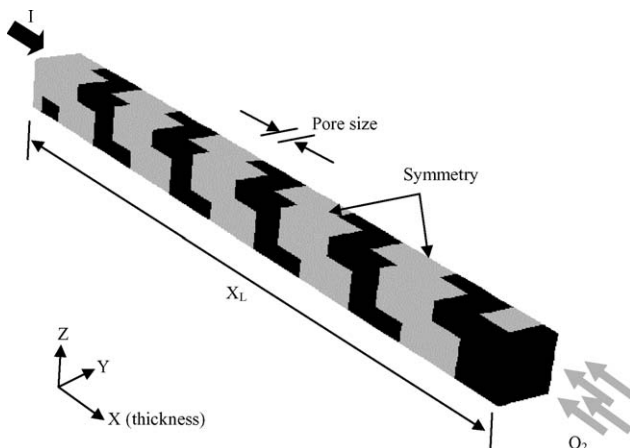
Fig. 4. Computational domain for the 3-D DNS model.

2.2.5. Solution procedure

The conservation equations, Eqs. (12) and (13) were discretized and solved using the commercial CFD software Fluent® [13]. The user defined functions (UDF) capability available in the Fluent® software was deployed to customize the source terms, given by Eqs. (17) and (18), as well as to solve the set of transport equations for the DNS calculation. For the baseline simulation, with nominal porosity of 0.375, a uniform mesh size of $42 \times 12 \times 12$ in the x-, y- and z-directions, respectively was found to be sufficient and convergence was considered achieved when the relative error, for each scalar, between two successive iterations reached 10^{-6}.

3. Results and discussion

3.1. 2-D model: kinetics- versus transport-limited regimes

In this section, the capabilities of the present DNS model are illustrated by comparing the simulation results with some experimental data. Further, the simulation results are analyzed to understand the various voltage losses from the cathode catalyst layer. Two sets of simulations are carried out using pure oxygen and air as oxidant, respectively, at various current densities. Oxygen and air are both fed at a pressure of 150 kPa when the cell is operated at 80 °C. In each set of calculations, a special case, in which the diffusion coefficient of O_2 in the gas phase is set to be infinitely large, is simulated to mimic the limiting case without the O_2 transport loss. Then, the two sets of results are compared with the corresponding experimental observations from the literature that are operated under similar conditions.

Polarization curves for various simulations are summarized in Fig. 5, including an analytical solution for the limiting case with both infinitely large proton conductivity in the electrolyte phase and O_2 diffusivity in the gas phase. In general, when the conductivities of both electronic phase and electrolyte phase become infinitely large, the overpotential becomes uniform across an electrode with a constant open-circuit potential. Then, if the mass diffusivity of the reactant is set to be infinitely large to
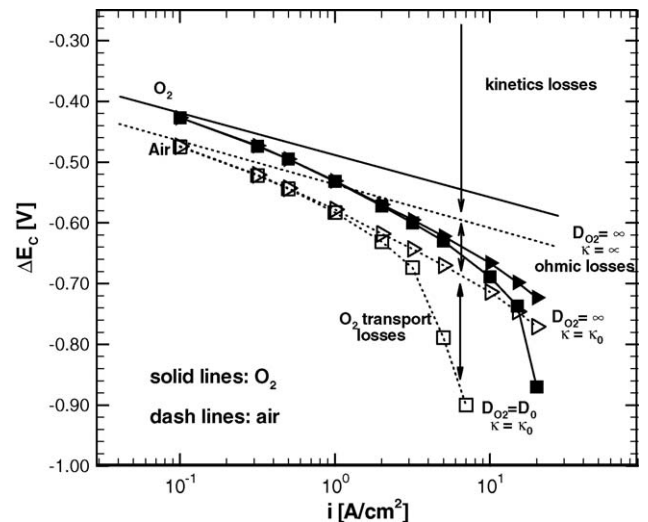
Fig. 5. Numerical predictions of the voltage losses in the cathode catalyst layer.

have a uniform concentration distribution, the electrochemical reaction rate will be uniform throughout the electrode. In this case, with Tafel kinetics for the ORR, the current balance for the catalyst layer yields:

$$i_0 \frac{c_{O_2}}{c_{O_2,ref}} \exp\left(-\frac{\alpha_c F}{RT}\eta\right) . A_{reaction} = i_d \cdot A_{cross} \qquad (22)$$

where $A_{reaction}$ stands for the total reaction area and A_{cross} represents the cross-sectional area on which the discharge current density, i_d, is applied. It should be noted that the concentration, c_{O_2} and overpotential, η, are constant in Eq. (22). A new parameter is defined to denote the area ratio as:

$$A_0 = \frac{A_{reaction}}{A_{cross}} \qquad (23)$$

The only voltage loss in this case, i.e. the kinetic loss is given by:

$$|\eta| = 2.303 \frac{RT}{\alpha_c F} \left[\log i_d - \log\left(A_0 i_0 \frac{c_{O_2}}{c_{O_2,ref}}\right)\right] \qquad (24)$$

In Eq. (24), the Tafel slope, $2.303(RT/\alpha_c F)$, is denoted by b and has the unit of mV/decade. In our simulation, b has the value of 70 mV/decade with α_c of 1.0 and an operation temperature of 80 °C. Eq. (24) states that in the absence of ohmic and transport losses, the cathode voltage drop will increase by 70 mV once the current density, i_d, increases by a factor of 10 or either the concentration, c_{O_2}, or the area ratio A_0 decreases by a factor of 10. In Fig. 5, the two straight lines show the pure kinetics losses for O_2 and air as oxidant, respectively. Clearly, since the mole fraction of O_2 in air is 0.21, there will be about 47 mV more losses when air is used instead of pure O_2 from the following calculation:

$$\Delta E_{O_2 \Rightarrow air} = 70 \cdot \log\left(\frac{100\%}{21\%}\right) = 47\,mV \qquad (25)$$

Fig. 5 also indicates that there are additional voltage losses when realistic electrolyte conductivity and O_2 diffusivity values are employed. These additional losses have been identified as ohmic losses and O_2 transport losses in the plot. To reveal these losses, the distributions of O_2 concentration and overpotential are plotted for the three different cases in Fig. 6. The corresponding operating current density is 3.16 A/cm^2 with air as the oxidant. When a realistic electrolyte conductivity value is used, the overpotential becomes non-uniform as shown by the dash line. The overpotential at the interface with the membrane, η_0, which stands for the total voltage loss in the catalyst layer, increases significantly from the dash-dot line to the dash line, when κ changes from infinity to 0.05 S/cm. When a realistic diffusivity value is incorporated, as shown by the solid line, η_0 becomes even larger due to the O_2 diffusion resistance. The value of η_0 could increase further if O_2 is depleted near the membrane–CL interface, which would occur at a higher current density. Correspondingly, these two additional voltage losses are marked as ohmic losses and O_2 transport losses in Fig. 5.

Experimental observations by Gasteiger et al. [14] are plotted in Fig. 7 in a similar fashion as in Fig. 5. The y-axis denotes
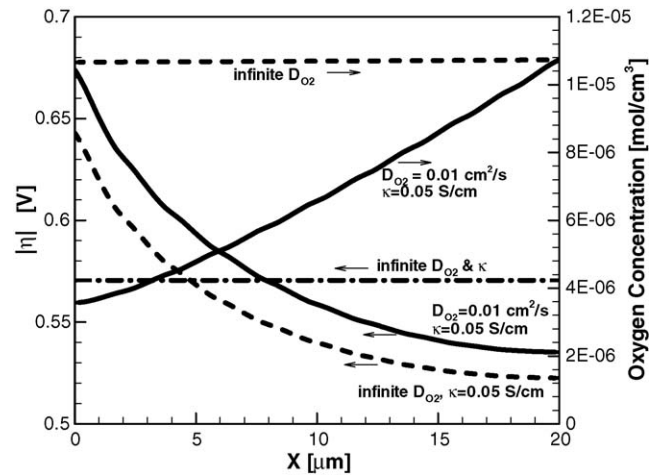
Fig. 6. Distributions of the overpotential and oxygen concentration across the thickness of the catalyst layer at current density of 3.16 A/cm^2.

the cathode IR-free potential by eliminating all the ohmic resistances. Different Pt-loadings are applied for both O_2 and air as the oxidant. It is observed that the curves simply shift down when the lower Pt-loading of 0.10 mg Pt/cm^2 is applied at the cathode. This is because the total reaction area decreases, subsequently, increasing the kinetics losses, as explained by Eq. (24).

Now, a comparison is made between the experimental observations (Fig. 7) and the predictions by the DNS calculations (Fig. 5). First, the kinetic losses in the two figures look different quantitatively. At the current density of 0.1 A/cm^2, the ORR kinetic losses in the experiments are about 370 mV assuming an equilibrium potential of 1.18 V corresponding to the air oxidant and 0.40 mg Pt/cm^2 catalyst loading in the cathode. However, the same losses in the DNS result are as large as 470 mV. This difference is mainly due to the small reaction surface area in the idealized structure used in simulations. It can be estimated that the total surface area ratio of Pt catalyst at the cathode is about 140 cm^2 Pt/cm^2 (electrode cross-sectional area) in the experiments when the 0.40/0.40 mg Pt/cm^2 Pt-loadings are used with typical dispersion surface area of Pt particles at 35 m^2/g Pt. On the other hand, this value in the model is only 10. Conse-
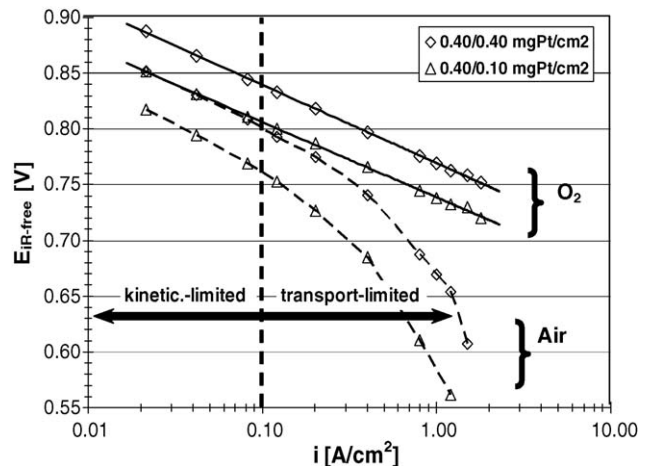
Fig. 7. Experimental observations of the voltage losses (Gasteiger et al. [14]).

quently, this difference by an order-of-magnitude in the surface area results in more voltage losses by as much as 80 mV in the simulations than that in the experiments. Furthermore, the Tafel slope obtained from the experiments is measured to be 66 mV/decade, while being 70 mV/decade in the simulations. This leads to another 30 mV more kinetic losses in the simulation results than that in the experimental data.

Secondly, the O_2 transport characteristics appear different between experiments and simulations, though they are in qualitative agreement. In Fig. 7, the transport-limited regime is identified when the current density is larger than 0.1 A/cm^2, which means the transport losses begin to appear in that region for air as the oxidant. In the simulations, when air is used as the oxidant, the transport of O_2 does not result in additional voltage drop until the current density is increased to 1 A/cm^2, where the deviation initiates. For pure oxygen as the oxidant, the diffusion becomes limiting at 5 A/cm^2, although the experiments have not been carried out at such a high rate. There are three factors that could explain why the O_2 transport losses appear later in the simulations than in the experiments. The most important reason is perhaps due to the better diffusion through the idealized geometry of pore spaces. Furthermore, in the present model, the blocking effect due to the product water has not been con-

sidered, which could also retard O_2 diffusion to some extent. Another possible explanation is that at the interface between the simulated catalyst layer and the gas diffusion layer (GDL), the O_2 concentration value is assumed the same as that at the channel inlet. Neglecting the diffusion resistance through the GDL could make the oxygen concentration at the CL–GDL interface significantly larger than a realistic value. Note that Stumper et al. [15] most recently measured an effective O_2 diffusivity across the CL–GDL composite medium that is nearly one order-of-magnitude lower than the gas counterpart. Nevertheless, DNS approach has been successfully utilized to delineate the various physical processes accounting for the different voltage drops in the cathode catalyst layer.

3.2. 3-D model: electrolyte potential and oxygen concentration fields

The catalyst layer with a thickness of 20 μm, porosity of 0.375 and pore size of ∼0.5 μm (i.e. macropores) is taken as a baseline case to perform the three-dimensional DNS model. The electrolyte phase potential and oxygen concentration fields predicted by the DNS model are illustrated in Figs. 8 and 9, respectively, under the operating current densities of 0.04,
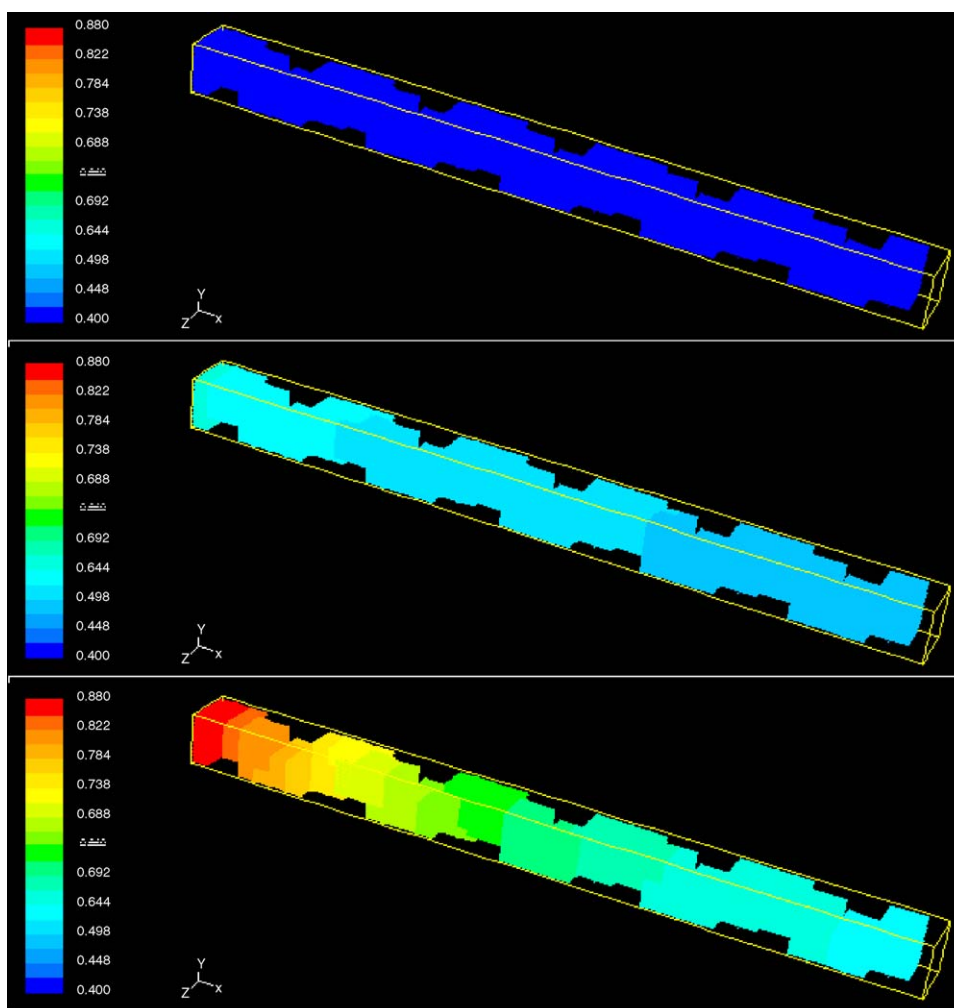
Fig. 8. Electrolyte potential (V) field at 0.04, 0.8 and 4 A/cm^2 current densities.
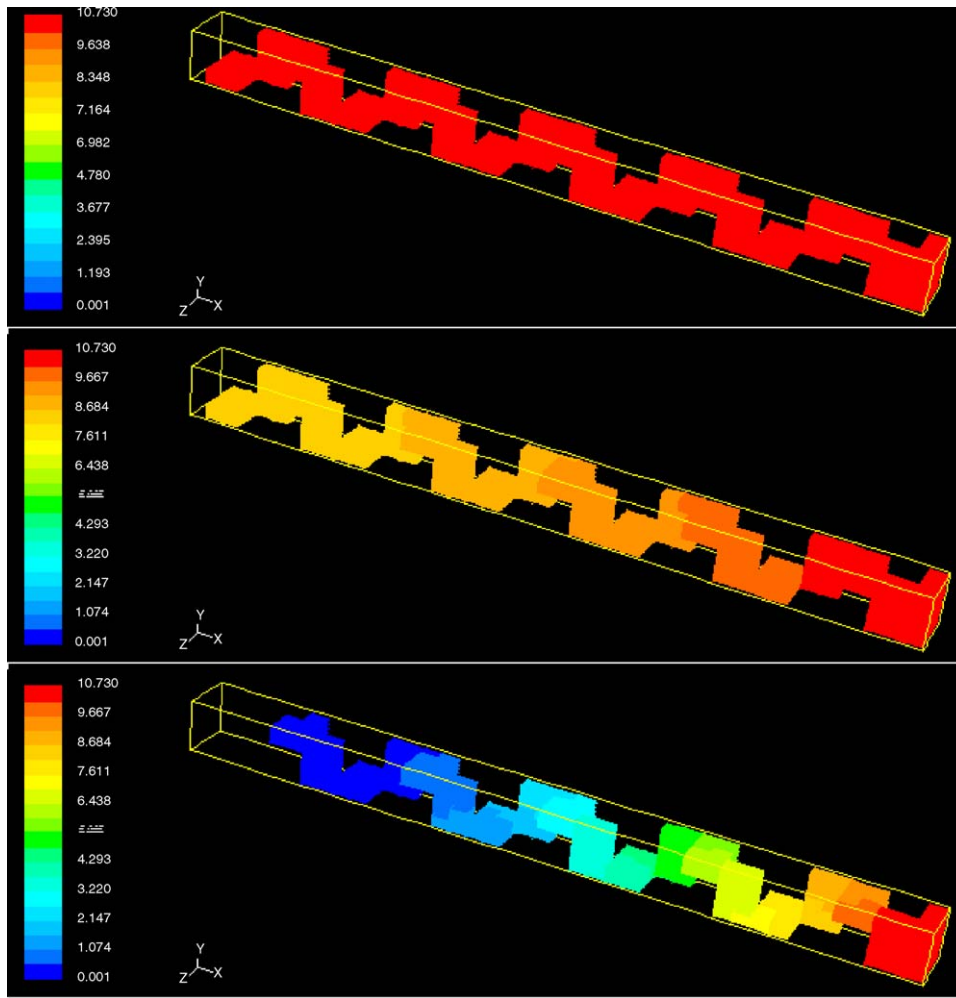
Fig. 9. Oxygen concentration (mol/m^3) field at 0.04, 0.8 and 4 A/cm^2 current densities.
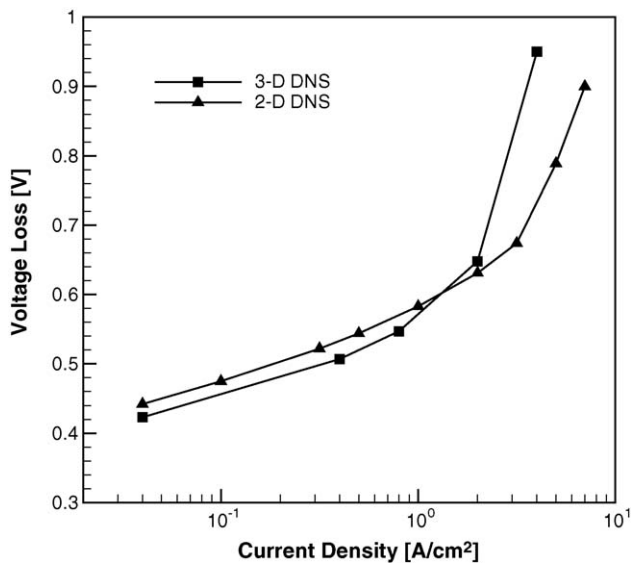
Fig. 10. Comparison of the polarization curves from the 2-D and 3-D DNS calculations.
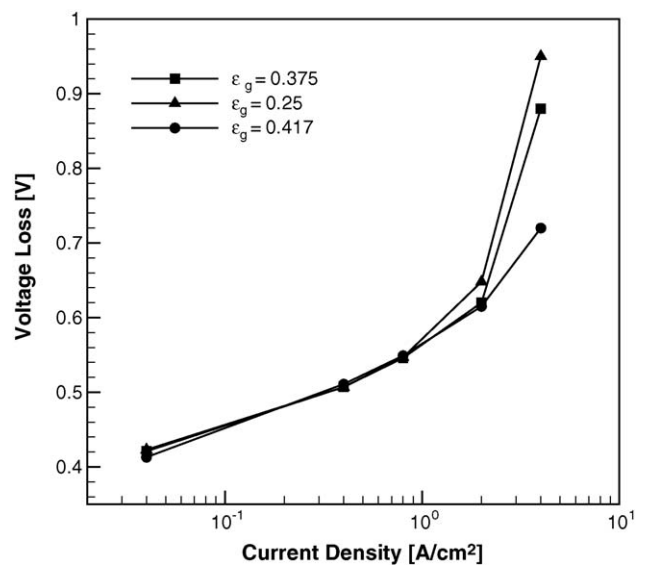
Fig. 11. Polarization curves with different porosities.

0.8 and 4 A/cm^2, corresponding to the kinetic control regime, mixed control regime and oxygen transport control regime, respectively.

At the small current density, the potential and oxygen concentration distributions are uniform, indicating a uniform reaction current across the catalyst layer. When the current density increases, the ohmic drop in the electrolyte phase makes the overpotential gradually increase toward the membrane–CL interface, causing the reaction to mostly concentrate at the front side of the catalyst layer. Correspondingly, oxygen concentration gradient begins to appear. After the current density is further raised, the front side becomes depleted of oxygen. Consequently, the total voltage loss, indicated by the overpotential at the interface with the membrane, increases dramatically not only because the proton migration through the oxygen-depletion region leads to considerable ohmic drop, but also because the reaction site is significantly reduced due to oxygen-depletion.

3.3. Comparison of the polarization curves between 2-D and 3-D simulations

The polarization curve generated by the three-dimensional DNS calculation is compared in Fig. 10 with the 2-D prediction.

It should be noted that the term "polarization curve" refers to the voltage loss versus current density curve throughout this article instead of the standard *I–V* curve, otherwise used widely in fuel cell literature. These two simulations are carried out under exactly the same conditions, except for the different geometries. It is also important to keep in mind that for comparison in Fig. 10, a porosity of 0.25 is used for the 3-D simulation, although the results from the baseline simulation with a porosity of 0.375 are reported in this work, if not otherwise mentioned specifically. As expected, the effects due to the three-dimensional geometry can be identified in two different regimes. In the kinetic control regime, voltage loss from the three-dimensional model is about 20 mV less than that from the two-dimensional model. Apparently, this is due to the increased phase interfacial area, which is one of the purposes to introduce the 3-D model. From the calculation, the total interfacial area for the 3-D geometry is around 20 times the electrode cross-sectional area, doubling the total area from the 2-D geometry. Therefore, it results in 20 mV less kinetics loss based on the 70 mV/decade Tafel slope as calculated earlier in the 2-D simulation. Another influence of the 3-D geometry is reflected in the transport of oxygen. Due to the more tortuous path in the 3-D structure, oxygen transport through the gas phase is restricted within the 3-D geometry. As
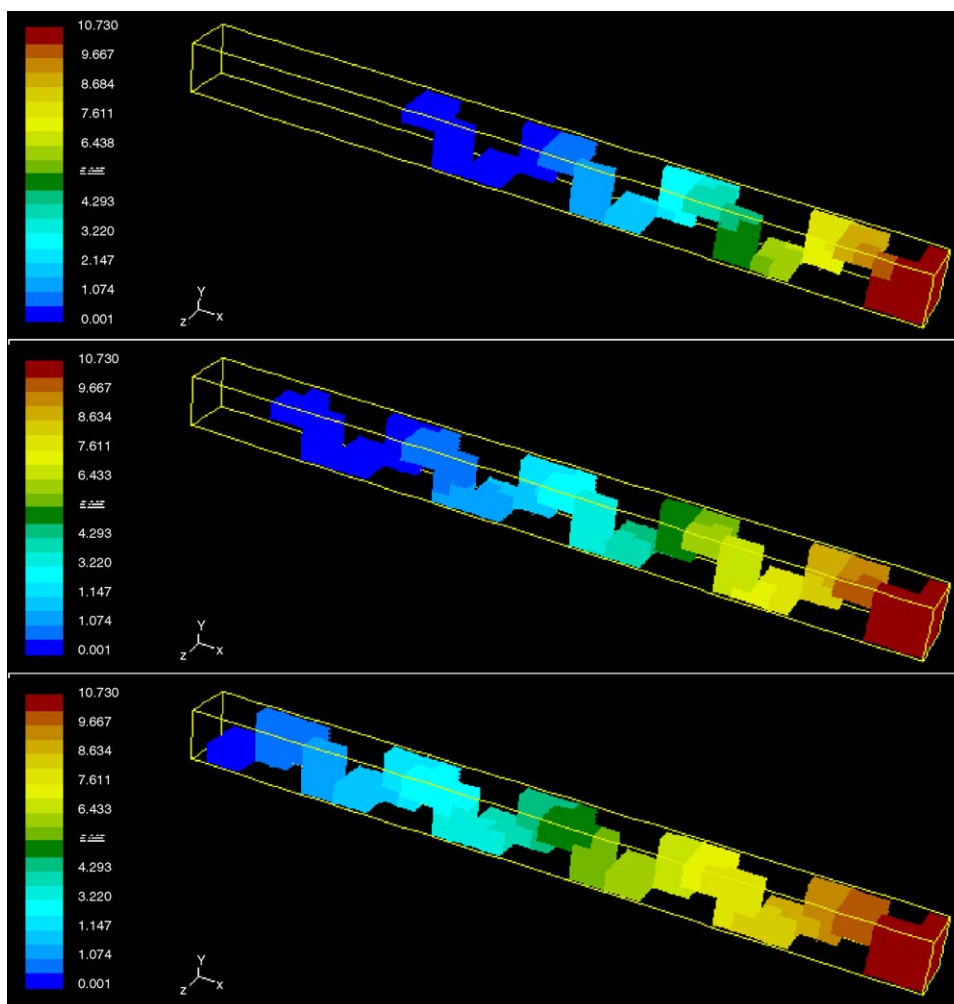
Fig. 12. Oxygen concentration (mol/m^3) contours at 4 A/cm^2 with different porosities.

a result, oxygen-depletion occurs earlier and the mass transport limiting current density decreases.

3.4. Porosity effect

Fig. 11 shows the effect of porosity on the polarization curve. Under small current densities in the kinetic regime, there is little difference in the cathode loss between different porosities because the respective interfacial areas for reaction are almost the same. This slight difference disappears at the moderate current densities with large porosity leading to higher ohmic drop due to the presence of less electrolyte phase volume fraction to conduct protons. However, when oxygen transport becomes dominant at high current densities, the performance of large porosity is greatly improved with considerable decrease of voltage loss due to the enhanced oxygen transport. This effect is clearly shown in Figs. 12 and 13.

Fig. 12 compares the oxygen concentration fields with different porosities operated at $4\,A/cm^2$. The comparison shows that when the porosity is decreased, the oxygen-depleted region near the membrane is expanded evidently. Obviously, this is due

to the reduced effective diffusivity from the smaller pore volume fraction. As a result of oxygen-depletion, the reaction zone is shifted to the back end of the catalyst layer (adjacent to the GDL), which is marked with the arrow in Fig. 13. With low porosity, the current has to flow through the electrolyte phase in the dominant part of the whole layer. This additional ohmic drop is the main reason why the low porosity leads to dramatically increased loss within the oxygen-depletion region.

3.5. Pore size and catalyst layer thickness effects

The pore size effect on the polarization curve is illustrated in Fig. 14. Three different pore sizes (0.5, 1.0 and 2.0 μm) have been simulated. The effect of increasing pore size is two-fold; first, the phase interfacial area is reduced. This is obviously observed from the polarization curves at small current densities, where higher kinetics drop results from the larger pore size. The doubled pore size brings about 20 mV more overpotential since the reaction area is reduced to one-half. The second effect is due to improved oxygen transport. The larger the pore size, the less severe is the oxygen transport limitation and better performance
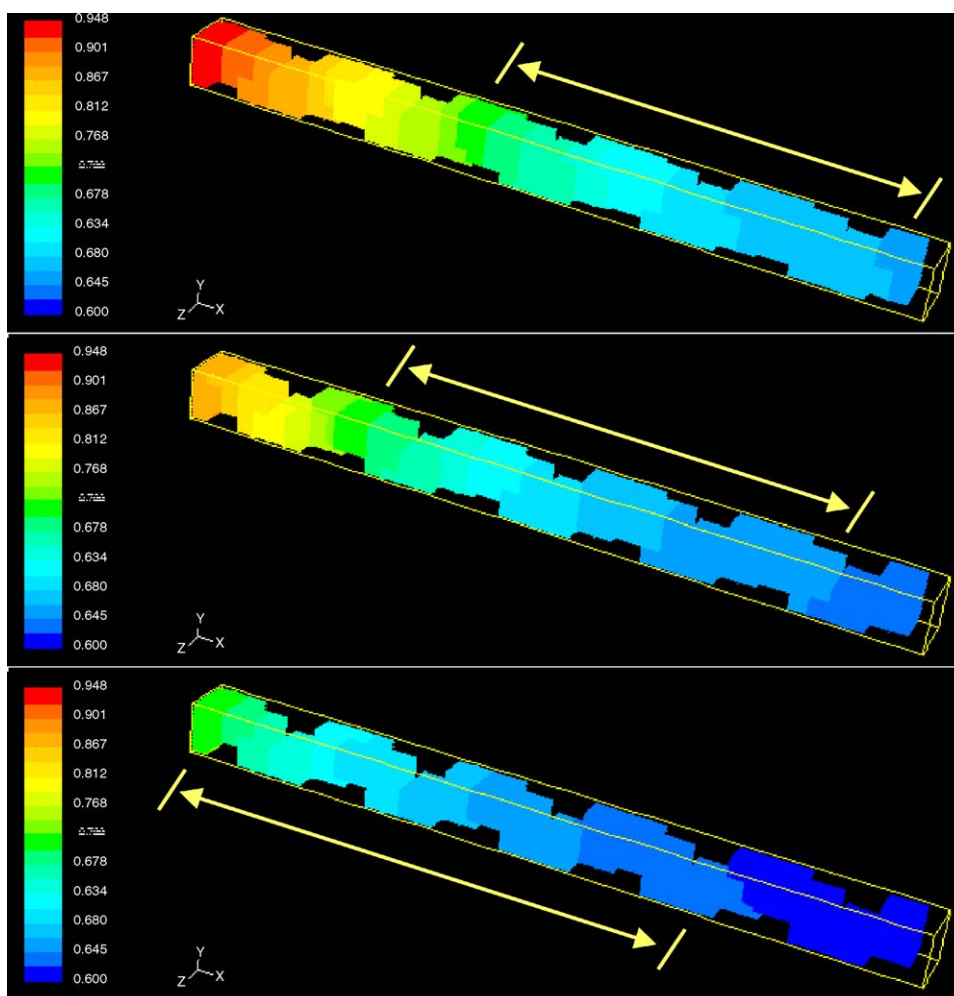
Fig. 13. Electrolyte potential (V) contours at $4\,A/cm^2$ with different porosities.
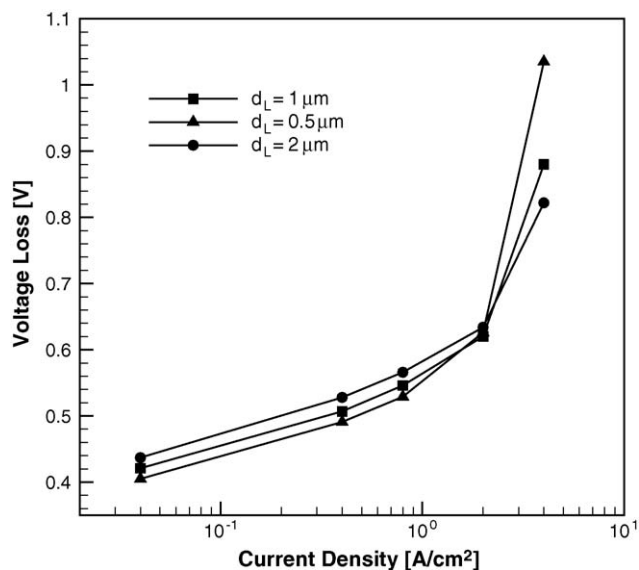
Fig. 14. Polarization curves with different pore sizes.

is obtained. This pore size effect reveals a unique advantage of the DNS model over the macrohomogenous model because the effective transport properties depend only on the porosity and tortuosity in the latter.

Fig. 15 shows that the catalyst layer thickness plays similar roles in the kinetic regime and mass transport limitation regime. The thicker catalyst layer provides more reaction site for transfer current, which would reduce the kinetic loss. At moderate current densities, more ohmic drop is generated for a thicker layer because the protons need to migrate through a longer electrolyte pathway. After oxygen-depletion occurs, additional ohmic drop is produced due to the expanded oxygen-depleted region within a thicker catalyst layer. Therefore, the thickness of the catalyst layer also needs to be optimized to combine the effects of the number of reaction site, ohmic drop and oxygen diffusion under the target operation.
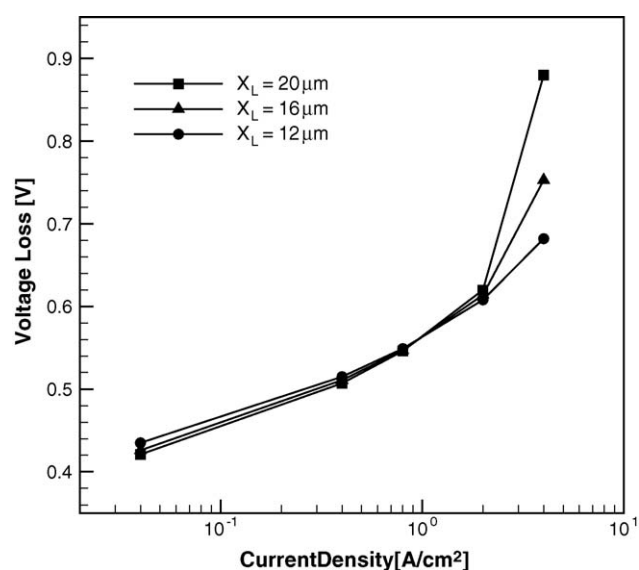
Fig. 15. Polarization curves with different catalyst layer thickness.

4. Conclusions

Pore-level description of the charge and oxygen transport is achieved through the systematic development of a direct numerical simulation model on regular 2- and 3-D realizations of the cathode catalyst layer microstructure. The 3-D microstructure provides a better delineation of the porous structure in terms of tortuosity and interfacial reaction surface area as compared to the 2-D structure. The advantage of the DNS model over the macrohomogeneous model is illustrated through resolving the microstructure and integrating its interaction with the underlying transport phenomena in the catalyst layer.

Acknowledgement

Appendix A. Nomenclature

a	specific interfacial area (cm^2/cm^3)
b	Tafel slope (mV/decade)
c_i	local concentration of species i (mol/m^3)
D_i	diffusion coefficient of species i (m^2/s)
f	phase function for the single domain approach
F	Faraday's constant (96,487 C/mol)
i_d	current density (A/cm^2)
i_0	exchange current density (A/cm^2)
j	reaction current density (A/cm^2)
p	pressure (Pa)
R	universal gas constant (8.314 J/(mol K))
S	source term in the governing equations
T	absolute temperature (K)
V_{oc}	open-circuit potential (V)
x	x-coordinate (μm)
y	y-coordinate (μm)

Greek letters

α_c	cathodic transfer coefficient
ε_κ	volume fraction of phase, k, in the catalyst layer
η	surface overpotential (V)
κ	electrolyte conductivity (S/m)
σ	conductivity of solid active material in an electrode (S/m)
ϕ_κ	electrical potential in phase k (V)

Subscripts and superscripts

e	electrolyte phase
g	gas phase
L	catalyst layer thickness
O_2	oxygen
ref	reference value
s	electronic phase
0	boundary value at the CL–GDL interface or initial/intrinsic value

References

[1] S. Gottesfeld, T.A. Zawodzinski, in: C. Tobias (Ed.), Advances in Electrochemical Science and Engineering, vol. 5, Wiley and Sons, New York, 1997.

[2] T.E. Springer, T.A. Zawodinski, S. Gottesfeld, J. Electrochem. Soc. 138 (8) (1991) 2334.

[3] D.M. Bernardi, M.W. Verbrugge, J. Electrochem. Soc. 139 (9) (1992) 2477.

[4] V. Gurau, H. Liu, S. Kakac, AIChE J. 44 (11) (1998) 2410.

[5] S. Um, C.Y. Wang, K.S. Chen, J. Electrochem. Soc. 147 (12) (2000) 4485.

[6] T.E. Springer, S. Gottesfeld, in: R.E. White (Ed.), Proceedings of Electrochemical Society, 1991.

[7] M. Eikerling, A.A. Kornyshev, J. Electroanal. Chem. 453 (1998) 89.

[8] M.L. Perry, J. Newman, E.J. Cairns, J. Electrochem. Soc. 145 (1) (1998) 5.

[9] C.Y. Wang, Chem. Rev. 104 (10) (2004) 4727.

[10] A.Z. Weber, J. Newman, Chem. Rev. 104 (10) (2004) 4679.

[11] L. Pisani, M. Valentini, G. Murgia, J. Electrochem. Soc. 150 (12) (2003) A1558.

[12] S.V. Patankar, Numerical Heat Transfer and Fluid Flow, Hemisphere, Washington, DC, 1980.

[13] Fluent 6.1 UDF Manual, Fluent Inc., NH, USA.

[14] H.A. Gasteiger, W. Gu, R. Makharia, M.F. Mathias, B. Sompalli, in: W. Vielstich, A. Lamm, H.A. Gasteiger (Eds.), Handbook of Fuel Cells—Fundamentals, Technology and Applications, vol. 3, Wiley, Chichester, 2003 (Chapter 46).

[15] J. Stumper, H. Haas, A. Granados, J. Electrochem. Soc. 152 (4) (2005) A837.